MNRAS **000**, 1–13 (2024) Preprint 19 March 2025 Compiled using MNRAS LaTeX style file v3.0

Mitigating numerical dissipation in simulations of subsonic turbulent flows

James Watt,[1]★ Christoph Federrath,[1]† Claudius Birke[2] and Christian Klingenberg[2]
[1]*Research School of Astronomy and Astrophysics, Australian National University, Cotter Road, Canberra, ACT 2611, Australia*
[2]*Department of Mathematics, University of Würzburg, Würzburg, Germany*

Accepted XXX. Received YYY; in original form ZZZ

ABSTRACT

Magnetohydrodynamic (MHD) simulations of subsonic (Mach number $<$ 1) turbulence are crucial to our understanding of several processes including oceanic and atmospheric flows, the amplification of magnetic fields in the early universe, accretion discs, and stratified flows in stars. In this work, we demonstrate that conventional numerical schemes are excessively dissipative in this low-Mach regime. We demonstrate that a new numerical scheme (termed 'USM-BK' and implemented in the FLASH MHD code) reduces the dissipation of kinetic and magnetic energy, constrains the divergence of magnetic field to zero close to machine precision, and resolves smaller-scale structure than other, more conventional schemes, and hence, is the most accurate for simulations of low-Mach turbulent flows. We first compare several numerical schemes/solvers, including Split-Roe, Split-Bouchut, USM-Roe, USM-HLLC, USM-HLLD, and the new USM-BK, on a simple vortex problem. We then compare the schemes/solvers in simulations of the turbulent dynamo and show that the choice of scheme affects the growth rate, saturation level, and viscous and resistive dissipation scale of the dynamo. We also measure the numerical kinematic Reynolds number (Re) and magnetic Reynolds number (Rm) of our otherwise ideal MHD flows, and show that the new USM-BK scheme provides the highest Re and comparable Rm amongst all the schemes compared.

Key words: MHD – turbulence – magnetic fields – methods: numerical

1 INTRODUCTION

Subsonic flows are ubiquitous in a wide range of physical systems, ranging from terrestrial applications to astrophysics. They appear in the study of turbine blade performance (Leggett et al. 2022), fusion and fission systems (Min et al. 2024), rotorcraft fuselages and ship airwakes (Park et al. 2022), ocean modelling (Tissot et al. 2023), stratified systems like stars (Kupka & Muthsam 2017), and the amplification of primordial magnetic fields (Wagstaff et al. 2014; Achikanath Chirakkara et al. 2021). Such subsonic flows are characterised by fluid velocities smaller than the speed of sound (also referred to as the low-Mach regime, where Mach number $M = v/c_\mathrm{s} < 1$ and v and c_s are flow velocity and sound speed, respectively). Being inherently non-linear and three-dimensional, these turbulent, complex systems are impossible to tackle via analytic calculations. Hence, they are studied through numerical simulations, a large class of which use finite volume discretisation and Godunov-based methods. While such methods are highly successful in modelling the transonic and the supersonic regime, they are subject to limitations in terms of efficiency in the subsonic regime. The artificial discontinuity created by the finite-volume method (FV method) at each cell interface creates spurious waves that lead to an overestimate of pressure, overwhelming the physical fluxes (see Guillard & Murrone 2004), leading to excessive dissipation in the low-Mach regime. Apart from this, the discretisation of the MHD equations introduces viscous terms as well (see Malvadi Shivakumar & Federrath (2023)). Both of these effects combined operate similar to physical viscosity (ν) and resistivity (η), and are referred to as artificial and numerical viscosity and resistivity.

These types of numerical/artificial viscosity and resistivity must be significantly lower than the physical viscosity and resistivity of the flow being modelled in an MHD simulation. Otherwise, features of the flow are smeared and the simulation results deviate significantly from the physical setting. Flow properties in MHD are determined primarily by the hydrodynamic and the magnetic Reynolds numbers, labelled Re and Rm, respectively. They are defined as

$$\mathrm{Re} = \frac{u\ell}{\nu}, \text{ and} \tag{1}$$

$$\mathrm{Rm} = \frac{u\ell}{\eta}, \tag{2}$$

where u and ℓ are the characteristic velocity and length scales of the flow, respectively. To accurately model a flow, the numerical Re and Rm must be larger than the physical Re and Rm of the flows being modelled.

Numerical dissipation arising from discretisation can be reduced by increasing the grid resolution and special techniques, like Adaptive Mesh Refinement (AMR) (Berger & Colella 1989). The effect of grid resolution on numerical viscosity and resistivity has been thoroughly studied by Malvadi Shivakumar & Federrath (2023). In this work, we focus on the dissipation originating from the artificial discontinuities created by the FV method in simulating subsonic flows. We test an extension of Waagan et al. (2011) introduced in Birke & Klingenberg (2023), which significantly reduces this dissipation.

In Section 2, we introduce the MHD equations. Section 3 describes

---

★ E-mail: James.Watt@anu.edu.au
† E-mail: christoph.federrath@anu.edu.au

our numerical methods and briefly summarises why simulations of subsonic flows are more dissipative and how Birke & Klingenberg (2023) overcome this difficulty. Section 4 presents simulations of the Balsara vortex (Balsara (2004), see also Leidi et al. (2022)) as a test case for a variety of numerical schemes, all at the same grid resolution, to demonstrate the effect of the choice of numerical scheme on artificial viscosity and resistivity and test if the new scheme provides an improvement over previous methods. In Section 5, we test the various numerical schemes on simulations of subsonic turbulent dynamos, which also have important astrophysical applications. We compare the effect of the numerical scheme on the time evolution and saturation of the dynamo, as well as the structure and turbulent MHD statistics of the system. We also measure the numerical Reynolds numbers of these otherwise ideal MHD (Re → ∞, Rm → ∞) simulations. We summarise our results in Section 6.

2 EQUATIONS OF MHD

The MHD equations are given as follows:

$$\frac{\partial \rho}{\partial t} + \nabla \cdot (\rho \boldsymbol{u}) = 0, \tag{3}$$

$$\frac{\partial}{\partial t}(\rho \boldsymbol{u}) + \nabla \cdot \left(\rho \boldsymbol{u} \otimes \boldsymbol{u} - \frac{1}{4\pi} \boldsymbol{B} \otimes \boldsymbol{B}\right) + \nabla p_{\mathrm{tot}} = \nabla \cdot (2\nu\rho \boldsymbol{S}) + \rho \boldsymbol{F}, \tag{4}$$

$$\frac{\partial e}{\partial t} + \nabla \cdot \left[(e + p_{\mathrm{tot}})\, \boldsymbol{u} - \frac{1}{4\pi}(\boldsymbol{B} \cdot \boldsymbol{u})\, \boldsymbol{B}\right] = \nabla \cdot \left[2\nu\rho \boldsymbol{u} \cdot \boldsymbol{S} + \frac{1}{4\pi}\eta \boldsymbol{B} \times (\nabla \times \boldsymbol{B})\right], \tag{5}$$

$$\frac{\partial}{\partial t}\boldsymbol{B} = \nabla \times (\boldsymbol{u} \times \boldsymbol{B}) + \eta \nabla^2 \boldsymbol{B}, \tag{6}$$

Here, $\rho, \boldsymbol{u}, p_{\mathrm{tot}} = p_{\mathrm{th}} + |\boldsymbol{B}|^2/(8\pi), \boldsymbol{B}, e = \rho e_{\mathrm{int}} + \rho|\boldsymbol{u}|^2/2 + |\boldsymbol{B}|^2/(8\pi)$, $S_{\mathrm{ij}} = (\partial_{\mathrm{i}} u_{\mathrm{j}} + \partial_{\mathrm{j}} u_{\mathrm{i}})/2 - (\delta_{\mathrm{ij}} \nabla \cdot \boldsymbol{u})/3$, ν, η denote the density, velocity, pressure (thermal plus magnetic), magnetic field, energy density (internal plus kinetic, plus magnetic), strain tensor, kinematic viscosity and magnetic resistivity, respectively. The system of equations is closed by an equation of state relating the thermal pressure (p_{th}) to the density (ρ).

The magnetic field also satisfies the divergence free constraint given by

$$\nabla \cdot \boldsymbol{B} = 0. \tag{7}$$

In the absence of physical viscosity and resistivity ($\nu = 0$ and $\eta = 0$), the system of partial differential equations described above takes the general conservative form

$$\frac{\partial \boldsymbol{U}}{\partial t} + \frac{\partial \boldsymbol{F}}{\partial x} + \frac{\partial \boldsymbol{G}}{\partial y} + \frac{\partial \boldsymbol{H}}{\partial z} = 0, \tag{8}$$

where $\boldsymbol{U}$ is a vector of conservative variables given by

$$\boldsymbol{U} = \left[\rho,\ \rho u_{\mathrm{x}},\ \rho u_{\mathrm{y}},\ \rho u_{\mathrm{z}},\ e,\ B_{\mathrm{x}},\ B_{\mathrm{y}},\ B_{\mathrm{z}}\right], \tag{9}$$

and $\boldsymbol{F}$, $\boldsymbol{G}$ and $\boldsymbol{H}$ are the fluxes given by

$$\boldsymbol{F} = [\rho v_{\mathrm{x}},\ \rho v_{\mathrm{x}}^2 + P + |\boldsymbol{B}|^2/8\pi - B_{\mathrm{x}}^2/4\pi,\ \rho v_{\mathrm{x}} v_{\mathrm{y}} - B_{\mathrm{x}} B_{\mathrm{y}}/4\pi,\ \rho v_{\mathrm{x}} v_{\mathrm{z}} - B_{\mathrm{x}} B_{\mathrm{z}}/4\pi,\ \left(e + P + |\boldsymbol{B}|^2/8\pi\right) v_{\mathrm{x}} - B_{\mathrm{x}}(\mathbf{v} \cdot \mathbf{B})/4\pi,\ 0,\ (v_{\mathrm{x}} B_{\mathrm{y}} - v_{\mathrm{y}} B_{\mathrm{x}}),\ -(v_{\mathrm{z}} B_{\mathrm{x}} - v_{\mathrm{x}} B_{\mathrm{z}})], \tag{10}$$

$$\boldsymbol{G} = [\rho v_{\mathrm{y}},\ \rho v_{\mathrm{x}} v_{\mathrm{y}} - B_{\mathrm{x}} B_{\mathrm{y}}/4\pi,\ \rho v_{\mathrm{y}}^2 + P + |\boldsymbol{B}|^2/8\pi - B_{\mathrm{y}}^2/4\pi,\ \rho v_{\mathrm{y}} v_{\mathrm{z}} - B_{\mathrm{y}} B_{\mathrm{z}}/4\pi,\ \left(e + P + |\boldsymbol{B}|^2/8\pi\right) v_{\mathrm{y}} - B_{\mathrm{y}}(\mathbf{v} \cdot \mathbf{B})/4\pi,\ 0,\ (v_{\mathrm{y}} B_{\mathrm{z}} - v_{\mathrm{z}} B_{\mathrm{y}}),\ -(v_{\mathrm{x}} B_{\mathrm{y}} - v_{\mathrm{y}} B_{\mathrm{x}})], \text{ and} \tag{11}$$

$$\boldsymbol{H} = [\rho v_{\mathrm{z}},\ \rho v_{\mathrm{x}} v_{\mathrm{z}} - B_{\mathrm{x}} B_{\mathrm{z}}/4\pi,\ \rho v_{\mathrm{y}} v_{\mathrm{z}} - B_{\mathrm{y}} B_{\mathrm{z}}/4\pi,\ \rho v_{\mathrm{z}}^2 + P + |\boldsymbol{B}|^2/8\pi - B_{\mathrm{z}}^2/4\pi,\ \left(e + P + |\boldsymbol{B}|^2/8\pi\right) v_{\mathrm{z}} - B_{\mathrm{z}}(\mathbf{v} \cdot \mathbf{B})/4\pi,\ 0,\ (v_{\mathrm{x}} B_{\mathrm{z}} - v_{\mathrm{z}} B_{\mathrm{x}}),\ -(v_{\mathrm{y}} B_{\mathrm{z}} - v_{\mathrm{z}} B_{\mathrm{y}})]. \tag{12}$$

3 NUMERICAL METHODS

3.1 Finite volume method

Eq. (8) can be solved using the finite-volume (FV) method. The FV method divides the computational domain into control volumes (grid cells) and integrates the governing equations over each volume, ensuring conservation of fluxes across cell boundaries. Fluxes at the interfaces are computed using Riemann solvers (such as Roe, HLLD, HLLC, etc). To improve accuracy, the physical state variables are reconstructed at the cell faces via linear or even higher-order reconstruction. Slope limiters are used to ensure that the reconstruction step does not introduce artificial maxima/minima. The temporal discretisation is performed using schemes such as Euler or Runge-Kutta methods and the time-stepping can be implemented in a split or unsplit fashion. The divergence of the magnetic field is constrained to zero up to machine precision using constrained transport (CT) (Yee 1966; Evans & Hawley 1988; Dai & Woodward 1998; Gardiner & Stone 2008), or kept at reasonably low levels by a divergence cleaning technique (Dedner et al. 2002).

3.2 Numerical dissipation

Discretisation of MHD equations gives rise to viscous terms that introduce numerical dissipation. This kind of numerical dissipation can be reduced by choosing a reconstruction method or a time stepper of higher order. However, finite volume methods also create an artificial discontinuity at each grid interface that gives rise to spurious waves. Since these artificial waves create pressure fluctuations of the order of the sonic Mach number M, they can overwhelm the physical flux in the simulations of low-Mach flows that have pressure fluctuations of the order M^2 (Guillard & Murrone 2004). This leads to excessive dissipation in low-Mach flows. Various methods have been explored to mitigate this issue, like pre-conditioning the Riemann problem at each interface to reduce the effect of discontinuities (Turkel 1999; Clerc 2000), or rescaling the dissipation term in the numerical flux to make it independent of the Mach number (Miczek et al. 2015; Minoshima & Miyoshi 2021; Leidi et al. 2022; Birke et al. 2023). Additionally, implicit-explicit methods, which use the Godunov-type method only for the slow dynamics in the PDE, so that the dissipation term does not scale with $O(1/M)$, are also a suitable approach for low-Mach problems (Klein 1995; Birke et al. 2024). In this work, we focus on the relaxation scheme by Birke & Klingenberg (2023) (referred to as the BK method), which resorts on rescaling the numerical flux in the low-Mach-number regime.

3.3 BK method

The core idea of the BK method is to construct an enlarged system of equations, including a relaxation term on the right-hand side, such that the new system is an approximation of the original system given in Section 2. Then the left-hand side of the relaxation system is solved using a Riemann solver followed by a projection of the solution back onto the original variables. Since there is some freedom in how the relaxation system is constructed, it is possible to tweak the solution of the pressure variable in the Riemann fan and fix the incorrect scaling of the pressure, while ensuring that the resulting Riemann solver satisfies a discrete entropy inequality. We point the reader to Birke & Klingenberg (2023) for further details on their relaxation scheme.

The fastest wave-speed in the Riemann fan of the BK relaxation scheme can be closely approximated by

$$\lambda_{\text{fastest}} = u + \frac{1}{2}\sqrt{\left(\frac{c_{\text{s}}^2}{M_{\text{BK}}^2} + c_{\text{A}}^2\right) + \sqrt{\left(\frac{c_{\text{s}}^2}{M_{\text{BK}}^2} + c_{\text{A}}^2\right)^2 - 4c_{\text{s}}^2 c_{\text{A;x}}^2}}, \quad (13)$$

where u is the fluid velocity, c_{s} is the sound speed, c_{A} is the Alfvén speed, $c_{\text{A;x}}$ is the Alfvén speed in the x-direction (direction along which the MHD equations are one-dimensionalised before solving the Riemann problem) and M_{BK} (the equivalent of ϕ in Eq. (14)–(16) in Birke & Klingenberg 2023) is defined as

$$M_{\text{BK}} = \min\left\{\max\left\{M_{\text{cut}}, \frac{u}{c_{\text{s}}}\right\}, 1\right\}. \quad (14)$$

The parameter M_{cut} is used to set a local cut-off Mach number below which the scheme does not reduce dissipation any longer by increasing the scheme-specific speed, thereby preventing division by small numbers in regions where the velocity is close to 0, which would lead to $\lambda_{\text{fastest}} \to \infty$ and the time-step $\Delta t \to 0$. In this work, we set M_{cut} equal to the reference Mach number ($\mathcal{M} = 0.1$ or 0.01) that we are simulating – the reference Mach number is a statistical (global) quantity describing the characteristic ratio of typical flow velocities to the sound speed in a given problem[1]. Note that for a conventional Riemann solver, like Roe or HLLD, $M_{\text{BK}} = 1$, and λ_{fastest} is a close approximation of the fastest wave speed in the Riemann fan of these conventional solvers.

The time-step restriction for stability is given by the Courant–Friedrichs–Lewy (CFL) condition,

$$\Delta t = \text{CFL}\frac{\Delta x}{\lambda_{\text{fastest}}}, \quad (15)$$

where Δx is the cell size. We use CFL = 0.5 throughout this work.

3.4 Numerical schemes in FLASH

We perform our simulations using a modified version of the FLASH code (Fryxell et al. 2000; Dubey et al. 2008) and compare several numerical schemes with different Riemann solvers. Some schemes utilise split time-stepping combined with Dedner-Marder cleaning (Marder 1987; Dedner et al. 2002) for magnetic field divergence control (Split-Roe and Split-Bouchut), while others adopt unsplit time-stepping on a staggered mesh with an upwind version of Lee's constrained transport scheme (Lee 2006) (USM-Roe, USM-HLLD, USM-HLLC, and USM-BK, where 'USM' stands for 'unsplit-staggered mesh'). All our schemes use the 2nd-order TVD (total variation diminishing) interpolation of data in space and time using the Hancock method (van Leer 1984). The details of the numerical schemes are summarised in Table 1.

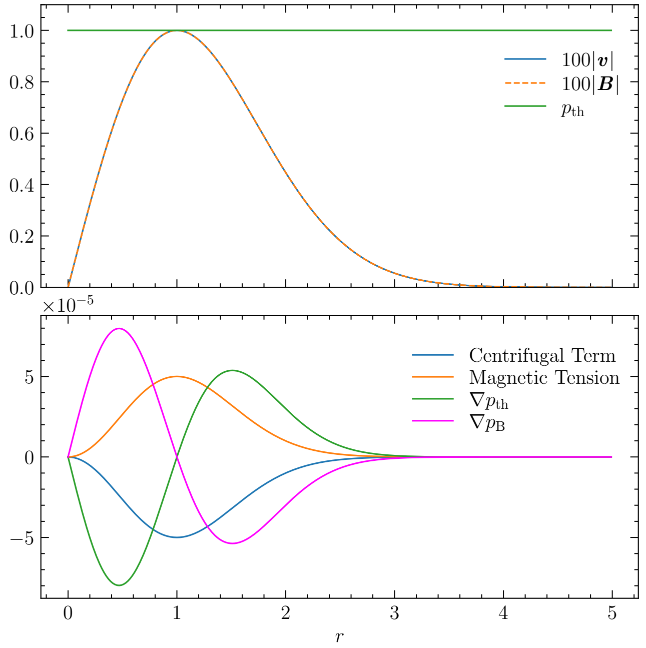

Figure 1. Top panel shows the radial profiles of velocity, magnetic field and pressure for the Balsara vortex, following Eqs. (16)–(18) for a sonic Mach number of $\mathcal{M} = 0.01$ and the ratio of the magnetic to the rotational kinetic energy $\beta_{\text{k}} = 1$. Note that the velocity and magnetic pressure profiles have been scaled by a factor of 100 for the sake of clarity. The scaled velocity profile touches the thermal pressure profile ($p_{\text{th}} \approx 1$) at $r = 1$ since $\mathcal{M} = 0.01$. The bottom panel shows that the centrifugal term $-(\boldsymbol{v} \cdot \nabla)\boldsymbol{v}$ is balanced by the magnetic tension $(\boldsymbol{B} \cdot \nabla)\boldsymbol{B}$, and the gradients of the thermal pressure (∇p_{th}) and the magnetic pressure (∇p_{B}) balance each other.

4 BALSARA VORTEX

The Balsara vortex (Balsara 2004) is an exact stationary solution of the ideal MHD equations in two dimensions, where the centrifugal force, magnetic tension, thermal pressure gradient, and magnetic pressure gradient are perfectly balanced. This configuration, which conserves kinetic and magnetic energies independently in the absence of dissipative forces, serves as an excellent test problem for evaluating energy conservation in MHD simulations. Discretisation errors and artificial discontinuities in finite-volume methods introduce numerical dissipation, leading to a loss of rotational and magnetic energy. Here we use the Balsara vortex to compare the energy conservation performance of various split and unsplit MHD solvers across different numerical schemes. While the dissipation we observe arises from a combination of numerical discretisation and the choice of numerical technique (like reconstruction method, Riemann solver, etc.) as well as the presence of artificial discontinuities, we use the same resolution for all the different schemes in Tab. 1, such that we can compare the dissipation arising from the latter.

---

[1] For instance, in turbulent flows, $\mathcal{M}$ is the standard deviation of M.

Table 1. Numerical schemes used in this work.

Scheme Name (1)	Split / Unsplit (2)	Riemann Solver (3)	$\nabla \cdot \boldsymbol{B}$ Method (4)	Electric Field Reconstruction (5)
Split-Roe	Split	Roe	Dedner-Marder cleaning	N/A
Split-Bouchut	Split	Bouchut	Dedner-Marder cleaning	N/A
USM-Roe	Unsplit	Roe	Constrained Transport	Lee-Upwind
USM-HLLD	Unsplit	HLLD	Constrained Transport	Lee-Upwind
USM-HLLC	Unsplit	HLLC	Constrained Transport	Lee-Upwind
USM-BK	Unsplit	BK	Constrained Transport	Lee-Upwind

Notes. Column (1): name of numerical scheme, (2): whether the scheme uses directionally split or unsplit updates, (3): Riemann solver – Roe (Roe 1981), Bouchut (Waagan et al. 2011), HLLD (Miyoshi & Kusano 2005), HLLC (Li 2005) or BK (Birke & Klingenberg 2023), (4): whether Dedner-Marder cleaning (Marder 1987; Dedner et al. 2002) or constrained transport (CT) (Yee 1966; Evans & Hawley 1988; Dai & Woodward 1998; Gardiner & Stone 2008) was used to handle the magnetic field divergence constraint, (5): Lee-upwind (Lee 2006) electric field reconstruction method, if applicable. All schemes use the 2nd-order Hancock (van Leer 1984) method for interpolation of data in space and time.

4.1 Initial conditions

The initial conditions for the Balsara vortex are given by

$$\boldsymbol{v} = \tilde{v}\,(-y\hat{\boldsymbol{x}} + x\hat{\boldsymbol{y}})\exp\left(\frac{1-r^2}{2}\right), \tag{16}$$

$$\boldsymbol{B} = \tilde{B}\,(-y\hat{\boldsymbol{x}} + x\hat{\boldsymbol{y}})\exp\left(\frac{1-r^2}{2}\right), \tag{17}$$

$$p_{\rm th} = 1 + \left[\frac{\tilde{B}^2}{2}(1-r^2) - \frac{\tilde{v}^2}{2}\right]\exp\left(1-r^2\right), \tag{18}$$

$$\rho = 1, \tag{19}$$

where $r^2 = x^2 + y^2$, and $\hat{\boldsymbol{x}}$ and $\hat{\boldsymbol{y}}$ are unit vectors in the x and y directions, respectively. We use $\tilde{v} = 0.01$, $\tilde{B} = 0.01$, and $\gamma = 5/3$. Here we define the reference Mach number ($\mathcal{M}$) as the maximum local Mach number (M) in the simulation domain. Our choice of parameters $\tilde{v}$, $\tilde{B}$ and γ gives $\mathcal{M} \approx 0.01$. The radial profiles of velocity, magnetic field and pressure are shown in Fig. 1.

4.2 Setup

We use a computational domain of $(x, y) \in [-5, 5]\times[-5, 5]$ and 64×64 grid cells with periodic boundary conditions for our simulations. The problem is made computationally harder by advecting the vortex along the diagonal of the computational grid with speed $\tilde{v}$. We run our simulations for one complete advection of the vortex across the diagonal, such that it ends up exactly at the starting position, i.e., at the coordinate origin. In this time interval, the vortex turns around 2.25 times.

4.3 Results and comparison of solvers

In order to quantify the amount of kinetic and magnetic energy dissipation, we calculate and compare the fraction of rotational and magnetic energy that the vortex has retained compared to their respective initial values. The rotational kinetic energy ($E_{\rm rot}$) is calculated as

$$E_{\rm rot} = \frac{1}{2}\rho\left[\left(v_{\rm x} - \frac{\tilde{v}}{2}\right)^2 + \left(v_{\rm y} - \frac{\tilde{v}}{2}\right)^2\right], \tag{20}$$

while the magnetic energy ($E_{\rm mag}$) is calculated as

$$E_{\rm mag} = \frac{1}{2}|\boldsymbol{B}|^2. \tag{21}$$

Fig. 2 shows the fraction of the rotational energy retained in the system at the end of one complete advection of the vortex. The energy has been normalised by the maximum local rotational energy

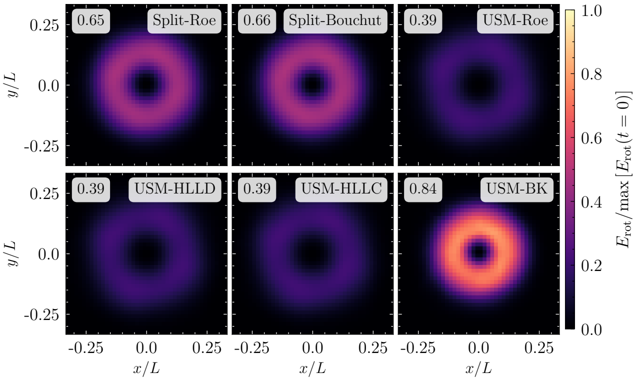

Figure 2. Rotational energy of the vortex after one advection diagonally through the computational domain for the six different numerical solver/scheme combinations (from left to right and top to bottom): Split-Roe, Split-Bouchut, USM-Roe, USM-HLLD, USM-HLLC, and USM-BK. The rotational energy has been normalised by the maximum rotational energy (at $r = 1$) at the beginning of the simulation ($t = 0$). The value in the top left corner of each panel shows the fraction of the total rotational energy left in the system compared to $t = 0$. We see that USM-BK outperforms all other schemes by retaining 84% of the rotational kinetic energy.

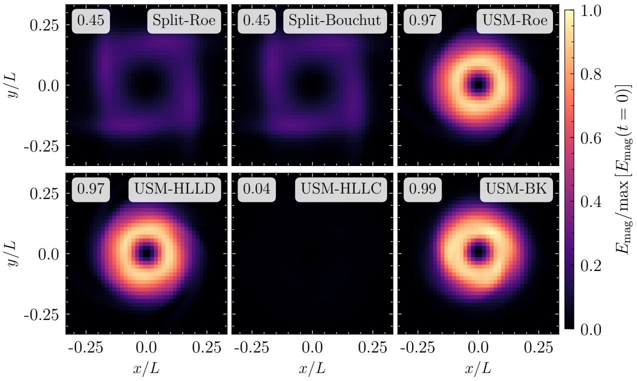

Figure 3. Same as Fig. 2, but for the magnetic energy. The value in the top left corner of each panel shows the fraction of the total magnetic energy left in the system after one complete box advection compared to $t = 0$. We find that the USM-BK scheme is also the best-performing scheme with respect to the magnetic energy, with only 1% of the initial energy dissipated. The Split schemes dissipate magnetic energy while damping the magnetic monopoles, while the 3-wave USM-HLLC scheme has dissipated almost all of the magnetic energy in the system.

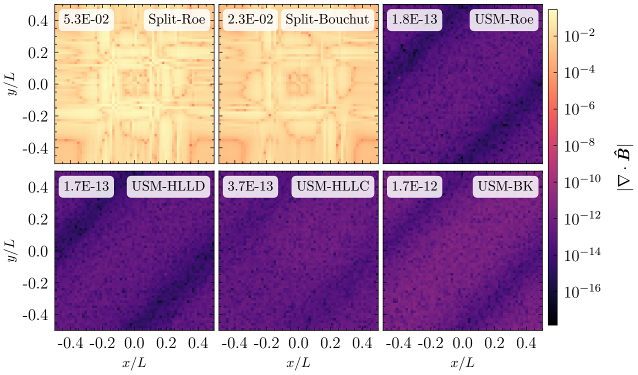

Figure 4. Same as Fig. 2, but for the divergence of the magnetic field, defined in a normalised fashion via Eq. (22), such that its magnitude can be compared to order unity. The inset on the top left in each panel shows the root-mean-squared value of $\nabla \cdot \hat{\boldsymbol{B}}$. The split schemes keep the value of $\nabla \cdot \boldsymbol{B}$ at reasonably low levels while the USM schemes maintain $\nabla \cdot \boldsymbol{B} = 0$ close to machine precision.

(at $r = 1$) present in the system at the beginning of the evolution. We find that the split schemes (Split-Roe and Split-Bouchut) retain around 65% of the kinetic energy, while the unsplit schemes (USM), except for the USM-BK, retain only 39% of the initial rotational kinetic energy. The new scheme (USM-BK; bottom right panel) performs the best, conserving 84% of the rotational energy.

Fig. 3 shows the same as Fig. 2, but for the magnetic energy. Split-Roe and Split-Bouchut lose more than half of their initial magnetic energy and significantly distort the vortex into a nearly square-shaped form. The increased dissipation is a consequence of the divergence-cleaning method, which also dissipates magnetic energy while damping the magnetic monopoles. USM-Roe, USM-HLLD, and USM-BK perform similarly well in conserving the magnetic energy, with USM-BK retaining 99% of the initial magnetic energy. These schemes introduce minor distortions in the shape of the vortex. At the same time, USM-HLLC, which considers only 3 waves in the Riemann solution, dissipates almost all the magnetic energy in the system.

Finally, we look at the divergence of the magnetic field. We define a normalised version of $\nabla \cdot \boldsymbol{B}$, as

$$\nabla \cdot \hat{\boldsymbol{B}} = \nabla \cdot \frac{\boldsymbol{B}}{B_{\mathrm{rms}} \Delta x}, \tag{22}$$

where B_{rms} is the root-mean-squared magnetic field integrated over the entire volume, and Δx is the side length of each grid cell. Fig. 4 shows $|\nabla \cdot \hat{\boldsymbol{B}}|$. The choice of Riemann solver does not play any significant role in constraining the divergence of the magnetic field to zero, however, all simulations using constrained transport (USM) perform much better compared to the divergence cleaning used in the split schemes. This is expected since divergence cleaning schemes do not enforce any particular discretisation of $\nabla \cdot \boldsymbol{B}$ to zero. They instead rely on diffusing and damping numerical magnetic monopoles. On the other hand, constrained transport is designed such that $\nabla \cdot \boldsymbol{B} = 0$ to machine precision by the construction of a particular stencil chosen to construct $\boldsymbol{B}$ from the electric field and to calculate $\nabla \cdot \boldsymbol{B}$.

5 APPLICATION TO MAGNETIC FIELD AMPLIFICATION IN LOW-MACH TURBULENCE

5.1 Introduction to the turbulent dynamo

Magnetic fields play an important role in a wide variety of astrophysical systems, including accretion disks (Penna et al. 2010; Boneva, D. V. et al. 2021), star formation (Choudhari 2015; Federrath 2015; Sharda et al. 2021), galaxies (Ruzmaikin et al. 1988; Beck & Wielebinski 2013), and the interstellar medium (Fletcher et al. 2011; Seta & Federrath 2022). The presence of strong magnetic fields is attributed to the amplification of seed fields by *turbulent dynamos*. Turbulent dynamos amplify magnetic fields exponentially over short timescales. This amplification is caused by a sequence of "stretching, twisting, folding, and merging" (Schekochihin et al. 2004; Brandenburg & Subramanian 2005; Federrath 2016) of magnetic field lines induced by turbulent motions in the plasma, leading to an increase in the density of magnetic field lines in a fluid packet.

5.2 Numerical method and setup

We solve Eqs. (3)–(7) in a periodic 3D box of length L, uniformly discretised with a grid of 256^3 cells. Turbulence is driven stochastically by the Ornstein-Uhlenbeck process (Eswaran & Pope 1988; Federrath et al. 2010) implemented in the publicly available code `TurbGen` (Federrath et al. 2022). The turbulence driving field is constructed here to be purely solenoidal (divergence free), using a Helmholtz decomposition in Fourier space, where we measure wave numbers (k) in units of $2\pi/L$. The driving is constrained to large scales, i.e., $k = [1, 3]$, following a parabolic Fourier spectrum, where the peak injection is at $k_{\mathrm{turb}} = 2$ and the driving amplitude falls off smoothly to zero at $k = 1$ and $k = 3$, respectively, as in previous works (e.g., Federrath et al. 2021). Using this turbulence driving method, we adjust the overall amplitude of the driver such that the turbulence reaches a target velocity dispersion $\sigma_v = \mathcal{M} c_{\mathrm{s}}$ on scale $\ell_{\mathrm{turb}} = L/k_{\mathrm{turb}} = L/2$, where c_{s} is the sound speed and $\mathcal{M}$ is the target turbulence Mach number. This defines the turbulence turnover timescale as $t_{\mathrm{turb}} = \ell_{\mathrm{turb}}/\sigma_v = L/(2\mathcal{M} c_{\mathrm{s}})$. Here we study sonic Mach numbers of $\mathcal{M} = 0.1$ and 0.01.

The box is initialised with a uniform density of fluid at rest and the sound speed is set to $c_{\mathrm{s}} = 1$, i.e., all speeds are measured relative to the sound speed. The strength and statistical properties of the turbulent dynamo are independent of the structure of the initial magnetic field (Seta & Federrath 2020), so we initialise a uniform magnetic field in the z-direction of the computational domain to obtain a reference Alfvén Mach number of $\mathcal{M}_{\mathrm{A}} = \sigma_v / c_{\mathrm{A}} = 10^9$ when the turbulence is fully developed. This corresponds to a very weak initial seed field that is subsequently amplified by the turbulent dynamo.

Finally, for the runs with the USM-BK scheme, we set the cut-off Mach number (see Eq. 14) to $M_{\mathrm{cut}} = \mathcal{M}$.

5.3 Results for Mach 0.1

In ideal-MHD, we set ν and η in Eqs. (3)–(7) to 0. However, as shown earlier, numerical dissipation is always present owing to finite cell discretisation (Malvadi Shivakumar & Federrath 2023) and due to the numerical scheme. Consequently, for excessively dissipative solvers, the results from numerical simulations can deviate significantly from the physical setting. In the following sections, we compare the effect of MHD solvers on the time evolution and morphology of the system and calculate the characteristic wave-numbers associated with

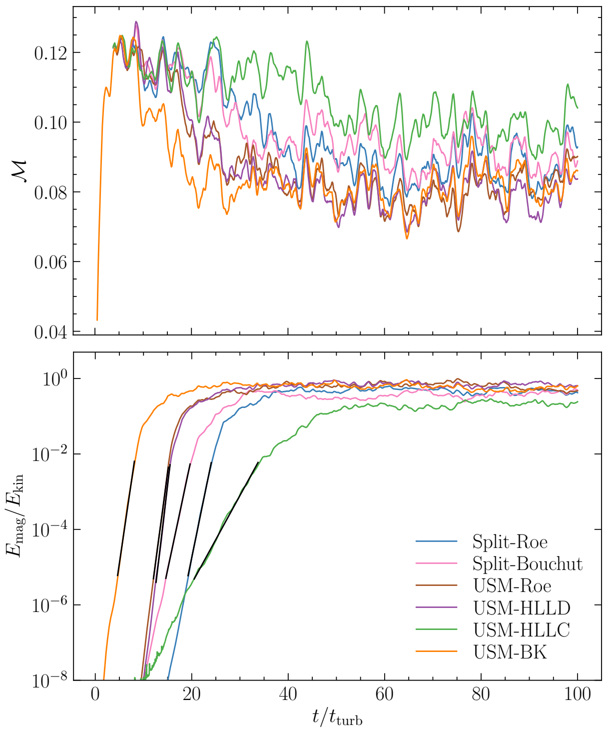

Figure 5. Time evolution of the sonic Mach number (top panel) and the ratio of magnetic to kinetic (turbulent) energy (bottom panel). The Mach number reaches the target value of $\approx$ 0.1 within $2t_{\mathrm{turb}}$, and during 3 and $10-30t_{\mathrm{turb}}$ (depending on the solver; labeled in the legend), the magnetic energy grows exponentially (see fitted solid lines in the bottom panel). Finally, once $E_{\mathrm{mag}}/E_{\mathrm{kin}} \gtrapprox 0.5$, the field saturates and the growth stops, coinciding with a $\approx 20\%$ drop in the Mach number (see top panel), due to the enhanced back-reaction of the field onto the flow. USM-HLLD, USM-Roe and USM-BK have the highest growth rate (see Table 2) since they are less dissipative. On the other hand, the 3-wave USM-HLLC has the smallest growth rate, and it shows the weakest dip in Mach number owing to its excessive dissipation of the magnetic energy.

numerical viscosity and resistivity at Mach 0.1. We run our simulations for a period of 100 t_{turb} to allow the magnetic field to saturate. However, we focus most of our analyses on the so-called 'kinematic phase', where the field does not have a strong back-reaction on the flow yet, and the field grows exponentially fast.

5.3.1 *Time evolution*

Fig. 5 shows the growth of the sonic Mach number ($\mathcal{M}$) in the top panel and the ratio of the magnetic energy to the kinetic energy ($E_{\mathrm{mag}}/E_{\mathrm{kin}}$) in the bottom panel. We see that the Mach number reaches the target value of 0.1 within 2 t_{turb}. It is followed by the kinematic phase, where the magnetic energy increases exponentially (up to $10-30\,t_{\mathrm{turb}}$, depending on the numerical scheme used). This is attributed to the turbulent motions of the fluid, which stretch, twist, fold, and merge the magnetic field lines, leading to an increase in their concentration. Finally, as the magnetic field strength increases, the Lorentz force back-reacts on the turbulent motion, suppressing further amplification and saturating the magnetic field. This back-reaction also lowers the Mach number by about 20%.

In order to measure the magnetic field dynamo growth rate, we fit the exponential model

$$\frac{E_{\mathrm{mag}}}{E_{\mathrm{kin}}} = Ae^{\Gamma t}, \tag{23}$$

in the kinematic phase, which we define as $5\times10^{-6} \le E_{\mathrm{mag}}/E_{\mathrm{kin}} \le 5\times10^{-3}$ (i.e., $E_{\mathrm{mag}} \ll E_{\mathrm{kin}}$), and Γ is the growth rate measured in units of t_{turb}^{-1}. The growth rates measured from the fits are listed in Table 2.

The USM-HLLC scheme exhibits an abnormally low growth rate. Consequently, the magnetic field and the Lorentz force is weaker compared to the other solvers and the sonic Mach number is higher. It also has a lower saturation level (see column 3 in Table 2). This behaviour is attributed to the excessive dissipation of magnetic energy by the HLLC solver (see bottom-middle panel in Fig. 3). In contrast, USM-HLLD, USM-Roe and USM-BK achieve the highest growth rates due to their reduced numerical dissipation. It is important to note that the growth rate depends on the magnetic Prandtl number (see Federrath et al. 2014), which, in turn, is determined by the ratio of the resistive to viscous dissipation wave-numbers (see Appendix A). Therefore, the growth rate is not a universal indicator of solver performance. For instance, USM-HLLD and UMS-Roe simulations exhibit higher effective Prandtl numbers (see Table 5), resulting in a slightly higher growth rate than that of USM-BK.

5.3.2 *Magnetic field structure*

Numerical dissipation also affects the morphology of the system. To get a qualitative idea of this in turbulent flows, we investigate the spatial distribution of the magnetic energy. Fig. 6 shows a slice of the magnetic energy normalised by the mean magnetic energy during the kinematic phase of the dynamo, when $E_{\mathrm{mag}}/E_{\mathrm{kin}} = 10^{-4}$. We see random fluctuations in the magnetic energy field with all the solvers, however, the morphology is markedly different in USM-HLLC (bottom-middle panel) and slightly different for Split-Roe and Split-Bouchut (first two panels). They smear the over-densities and the under-densities in the field over larger regions. As mentioned earlier, the dissipation in the Split schemes is attributed to divergence-cleaning, while that in USM-HLLC is a result of its consideration of fewer waves in the Riemann solution. In contrast, USM-HLLD and USM-BK display fine, small-scale structures. We quantitatively analyse the differences between the various schemes in the next section.

5.3.3 *Spectral analysis*

In subsonic turbulence, energy cascades from larger scales to smaller scales until it reaches a scale where it is dissipated due to the effects of viscosity and resistivity (e.g., Frisch 1995). This takes place through the breaking-up of large eddies into smaller eddies. The wave-numbers where viscosity and resistivity act are called viscous dissipation wave-number k_{ν}, and resistive dissipation wave-number k_{η}, respectively.

We calculate the power spectrum of the kinetic energy averaged over the kinematic phase (as defined in Section 5.3.1) to measure the viscous dissipation wave-number. We follow the power spectrum model used in Malvadi Shivakumar & Federrath (2023) and fit the kinetic spectrum from $k \ge 3$ to exclude the turbulence driving scales. The upper limit of the fit is set to $k_{\mathrm{max}} = N/8 = 32$, where N is the number of grid cells, to exclude spurious effects that arise on scales smaller than a few grid cells.

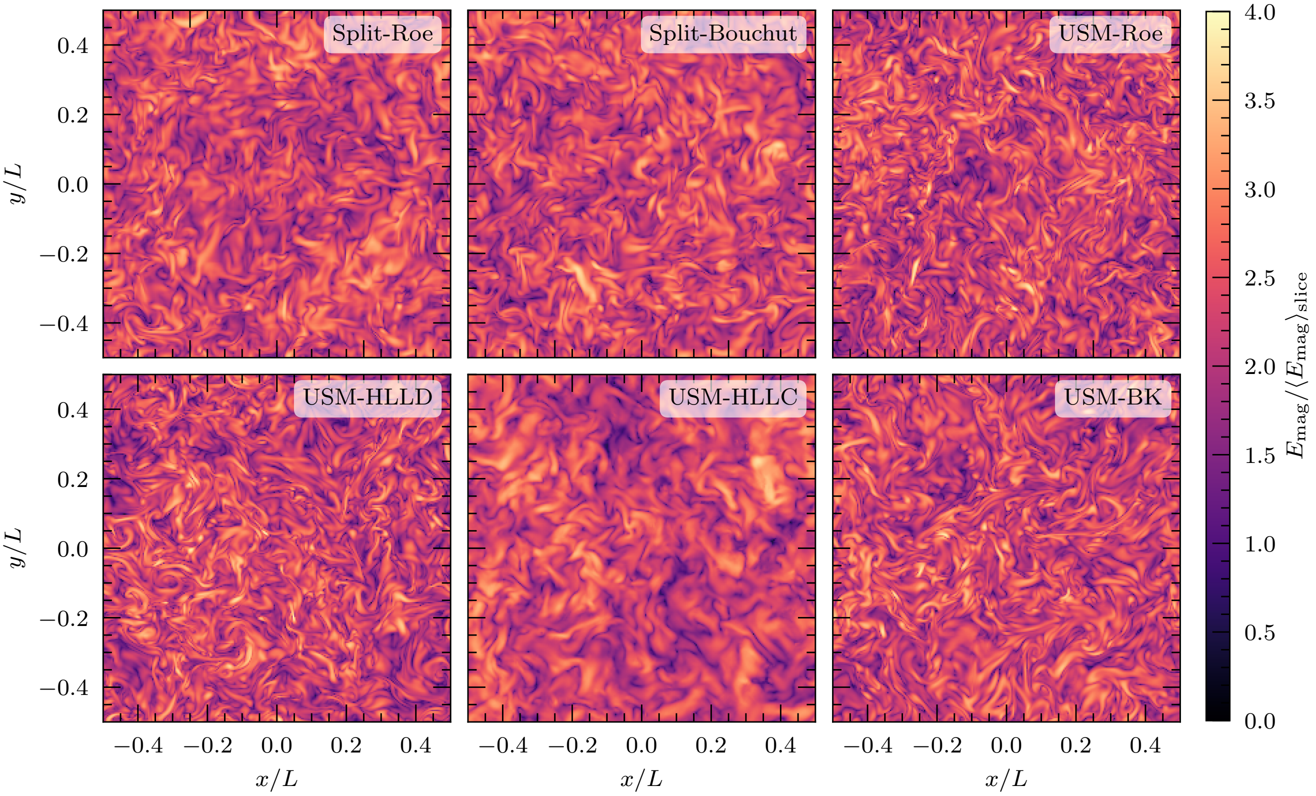

Figure 6. A slice of the magnetic energy normalised by the mean magnetic energy during the kinematic phase of the dynamo, when $E_{\rm mag}/E_{\rm kin} = 10^{-4}$, emphasising its spatial distribution. The more dissipative Split schemes and USM-HLLC smear features over large-length scales while USM-Roe, USM-HLLD and USM-BK capture finer structures.

The kinetic energy power spectrum ($P_{\rm kin}$) in the subsonic regime is modelled as

$$P_{\rm kin}(k) = A_{\rm kin}\left[\left(\frac{k}{k_{\rm bn}}\right)^{-1.7} + \left(\frac{k}{k_{\rm bn}}\right)^{p_{\rm bn}}\right]\exp\left[-\left(\frac{k}{\tilde{k}_\nu}\right)^{p_\nu}\right], \tag{24}$$

where $A_{\rm kin}$ is the amplitude, $k_{\rm bn}$ is the scale of energy accumulation due to the bottleneck effect (Falkovich 1994; Frisch 1995; Schmidt et al. 2004; Verma & Donzis 2007), $p_{\rm bn}$ characterises the strength of the bottleneck effect, and p_ν characterises the sharpness of the transition into dissipation. The viscous dissipation wave-number as defined in Kriel et al. (2022) is related to $\tilde{k}_\nu$ and $p_{\rm bn}$ by

$$k_\nu = \tilde{k}_\nu^{1/p_\nu}. \tag{25}$$

We point the reader to Malvadi Shivakumar & Federrath (2023) and references therein for the motivation behind this model.

To find the characteristic resistive dissipation wave-number (k_η), we follow the definition in Kriel et al. (2023), using the electric current ($\sim \nabla \times \boldsymbol{B}$) power spectrum. Since Ohmic dissipation is proportional to current, k_η is defined as the wave-number where the current attains a maximum.

The power spectra of kinetic energy, magnetic energy and current are shown in Fig. 7, and the fit parameters and the measured characteristic dissipation wave-numbers (k_ν and k_η) are given in Table 2. For the kinetic spectra, the dissipation scales are similar for all solvers except USM-BK, which shows dissipation at larger wave-numbers (an ≈ 17% difference compared to USM-HLLD). For the current spectra, we see that USM-HLLD marginally outperforms USM-BK (an ≈ 12% difference). We also see that the dissipation scale for HLLC lies at very small wave-numbers, i.e., it induces numerical dissipation effects at much larger lengths scales, smearing out small-scale features. Thus, it is particularly unsuitable for modelling MHD flows.

5.3.4 *Numerical Reynolds numbers*

Since numerical dissipation is always present in MHD simulations, the simulated flows have a finite numerical hydrodynamic Reynolds number (Re) and magnetic Reynolds number (Rm), in contrast to a perfectly ideal setting, where these would be infinite, because $\nu = \eta = 0$ in the MHD equations. Appendix A describes the procedure for obtaining Re and Rm from the characteristic dissipation scales, using the key relations,

$$\mathrm{Re} = \left(\frac{k_\nu}{c_{\rm Re}\, k_{\rm driving}}\right)^{4/3}, \tag{26}$$

$$\mathrm{Pm} = \left(\frac{k_\eta}{c_{\rm Pm}\, k_\nu}\right)^{2}, \text{ and} \tag{27}$$

$$\mathrm{Rm} = \mathrm{Re} \times \mathrm{Pm}, \tag{28}$$

where $c_{\rm Re} = 0.025^{+0.005}_{-0.006}$ and $c_{\rm Pm} = 2.3^{+0.8}_{-0.5}$.

Table 3 lists the values of the effective Re, Rm, and Pm for the Mach 0.1 simulations, for each numerical scheme. The measured values of Re range between 630^{+290}_{-150} and 810^{+400}_{-240} (an ≈ 30% variation), while Rm values vary between 1400^{+1200}_{-700} and 6300^{+5400}_{-3000} (a

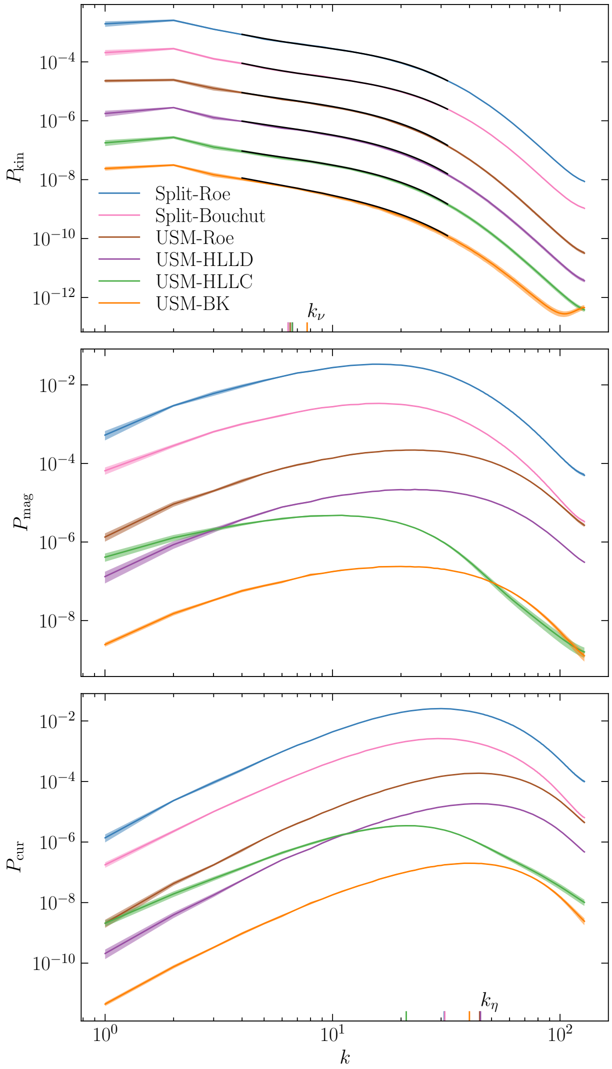

Figure 7. Time-averaged kinetic power spectra (top panel), magnetic power spectra (middle panel), and current power spectra (bottom panel) for various solvers. The spectra are multiplied for every solver except Split-Roe by a factor of 0.1 relative to the next solver in the legends. The black lines in the kinetic power spectra are the fits to the model given in Eq.(24). The viscous dissipation scale and resistive dissipation scale are marked on the x-axis. The viscous dissipation scales are clustered around each other for all solvers, however, the resistive dissipation scale measurements clearly show that HLLC is not suitable for MHD simulations since it is dissipative at very large length scales.

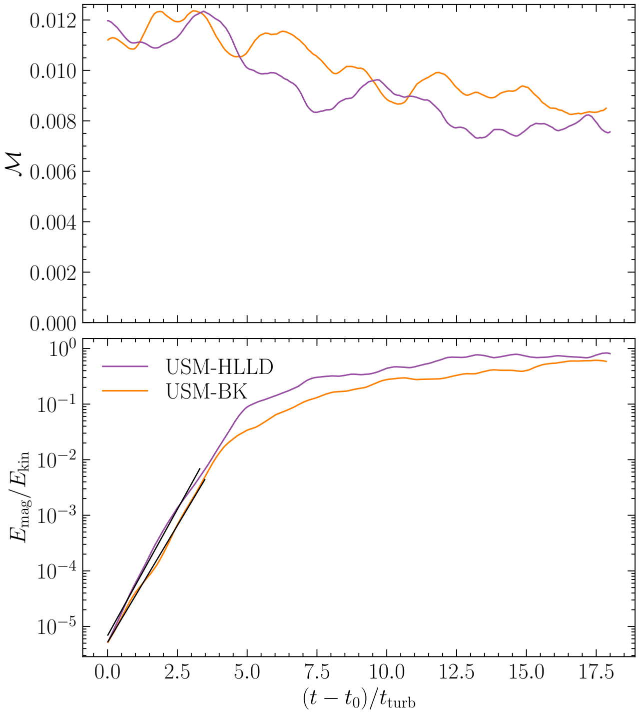

Figure 8. Similar to Fig. 5, but for Mach 0.01, comparing the best-performing solvers from the previous comparison at Mach 0.1, namely USM-BK (orange) and USM-HLLD (purple). Note that the x-axis shows $(t - t_0)/t_{\rm turb}$, where t_0 is chosen such that both runs start at the same $E_{\rm mag}/E_{\rm kin}$ to facilitate the comparison.

striking ≈ 350% variation attributable to the choice of the numerical scheme). The Pm values (which can be calculated from Re and Rm) vary between $2.1^{+1.6}_{-1.0}$ and $9.9^{+7.0}_{-4.6}$ (an ≈ 370% variation). We see that the USM-BK scheme shows the highest Re (810^{+400}_{-240} compared to 640^{+330}_{-200} for USM-HLLD, the next-highest value). This implies that USM-BK has the least dissipation of kinetic energy in the low-Mach regime among the solvers/schemes compared. We further find that USM-HLLD and USM-Roe have a higher Pm than USM-BK ($9.4^{+7.3}_{-4.4}$ and $9.9^{+7.0}_{-4.6}$ for USM-HLLD and USM-BK, respectively, compared to $5.6^{+4.2}_{-2.6}$ for USM-BK). As the dynamo growth rate depends on Re as well as Pm (see Federrath et al. 2014), these measurements of Pm explain why USM-BK has a somewhat smaller growth rate (c.f., Fig. 5 and Tab. 2) compared to USM-HLLD, despite being the least dissipative solver.

5.4 Results for Mach 0.01

We have already established in the Balsara vortex test (c.f., Sec. 4) that the schemes using Dedner-Marder cleaning do not perform very well in constraining the divergence of the magnetic field to zero. From our analysis of the electric current power spectra, it is quite clear that HLLC is not suitable for low-Mach simulations due to its large viscous dissipation length scale. Based on our study of energy conservation and the current power spectra, we can conclude that USM-HLLD and USM-BK have been the best-performing solvers so far, showing comparable results. Given that many astrophysical processes, such as stratified stellar flows (see Kupka & Muthsam 2017) and early-Universe turbulent dynamos (see Achikanath Chirakkara et al. 2021), involve highly subsonic flows with Mach numbers below 10^{-2}, we test these schemes further by running a turbulent dynamo simulation at Mach 0.01. Since our focus is on the kinematic stage of the dynamo (which we use to obtain solver properties), we stop our simulations close to the onset of saturation.

5.4.1 Time evolution

Fig. 8 shows the evolution of the Mach number and the ratio of magnetic energy to kinetic energy with time. The plots have been shifted so that both simulations have the same starting ratio of the kinetic energy to the magnetic energy, facilitating the comparison, as the initial conditions are not relevant for the turbulent dynamo (Seta & Federrath 2020; Beattie et al. 2023). The features are similar to

Table 2. Mach 0.1 turbulent dynamo measurements.

Name (1)	$\Gamma(t_{\mathrm{turb}}^{-1})$ (2)	$(E_{\mathrm{mag}}/E_{\mathrm{kin}})_{\mathrm{sat}}$ (3)	p_{bn} (4)	k_{bn} (5)	$\tilde{k}_\nu$ (6)	p_ν (7)	k_ν (8)	k_η (9)
Split-Roe	$1.43^{+0.01}_{-0.01}$	$0.48^{+0.07}_{-0.07}$	$0.92^{+0.09}_{-0.07}$	$5.5^{+0.3}_{-0.3}$	$5.9^{+0.1}_{-0.2}$	$1.0^{+0.1}_{-0.1}$	$6.3^{+0.1}_{-0.2}$	31^{+1}_{-1}
Split-Bouchut	$1.39^{+0.01}_{-0.01}$	$0.40^{+0.06}_{-0.06}$	$1.01^{+0.10}_{-0.08}$	$5.8^{+0.3}_{-0.3}$	$5.9^{+0.1}_{-0.2}$	$1.0^{+0.1}_{-0.1}$	$6.3^{+0.1}_{-0.2}$	31^{+1}_{-2}
USM-Roe	$2.20^{+0.01}_{-0.01}$	$0.66^{+0.13}_{-0.13}$	$0.42^{+0.28}_{-0.24}$	$4.0^{+0.8}_{-0.7}$	$6.8^{+1.7}_{-1.9}$	$1.0^{+0.1}_{-0.1}$	$6.4^{+0.6}_{-0.9}$	44^{+2}_{-1}
USM-HLLD	$2.48^{+0.01}_{-0.01}$	$0.69^{+0.09}_{-0.09}$	$0.35^{+0.35}_{-0.29}$	$3.9^{+0.7}_{-0.6}$	$7.1^{+2.2}_{-2.7}$	$1.0^{+0.1}_{-0.1}$	$6.5^{+0.6}_{-1.2}$	45^{+1}_{-2}
USM-HLLC	$0.54^{+0.01}_{-0.01}$	$0.21^{+0.04}_{-0.04}$	$0.36^{+0.38}_{-0.29}$	$4.1^{+1.0}_{-0.7}$	$7.4^{+2.1}_{-2.5}$	$1.1^{+0.1}_{-0.1}$	$6.5^{+0.7}_{-1.0}$	21^{+1}_{-2}
USM-BK	$2.00^{+0.01}_{-0.01}$	$0.58^{+0.10}_{-0.10}$	$-0.13^{+0.37}_{-0.30}$	$4.5^{+1.5}_{-1.0}$	$8.8^{+2.4}_{-2.8}$	$1.1^{+0.1}_{-0.1}$	$7.6^{+1.0}_{-1.1}$	40^{+1}_{-0}

Notes. All parameters except the saturation value of the ratio of the magnetic energy to the kinetic energy (column 3) were measured/derived by averaging over the kinematic phase of the dynamo when $5 \times 10^{-6} \leq E_{\mathrm{mag}}/E_{\mathrm{kin}} \leq 5 \times 10^{-3}$. Columns: (1) Name of the numerical scheme as described in Table 1. (2) Growth rate in units of t_{turb}^{-1}. (3) Average value of the ratio of the magnetic energy to the kinetic energy in the saturation phase of the dynamo ($t > 60 t_{\mathrm{turb}}$). (4) Exponent of the bottleneck effect in the kinetic spectrum. (5) Scaling wave-number of the bottleneck effect. (6) Viscous dissipation wave-number if $p_\nu = 1$. (7) Exponent of the dissipation term of P_{kin}. (8) Viscous dissipation wave-number. (9) Resistive dissipation wave-number.

Table 3. Mach 0.1 turbulent dynamo effective Reynolds numbers.

Name (1)	Re (2)	Rm (3)	Pm (4)
Split-Roe	$6.3^{+2.9}_{-1.5} \times 10^2$	$3.0^{+2.5}_{-1.5} \times 10^3$	$4.7^{+2.9}_{-2.2}$
Split-Bouchut	$6.4^{+2.7}_{-1.5} \times 10^2$	$3.0^{+2.5}_{-1.4} \times 10^3$	$4.6^{+2.9}_{-2.0}$
USM-Roe	$6.4^{+2.9}_{-1.8} \times 10^2$	$6.3^{+5.4}_{-3.0} \times 10^3$	$9.9^{+7.0}_{-4.6}$
USM-HLLD	$6.4^{+3.3}_{-2.0} \times 10^2$	$6.1^{+5.1}_{-3.0} \times 10^3$	$9.4^{+7.3}_{-4.4}$
USM-HLLC	$6.5^{+3.2}_{-1.9} \times 10^2$	$1.4^{+1.2}_{-0.7} \times 10^3$	$2.1^{+1.6}_{-1.0}$
USM-BK	$8.1^{+4.0}_{-2.4} \times 10^2$	$4.6^{+3.7}_{-2.2} \times 10^3$	$5.6^{+4.2}_{-2.6}$

what we see at Mach 0.1 (cf., Fig. 5). We define the kinematic phase as in Section 5.3.1 ($5 \times 10^{-6} \leq E_{\mathrm{mag}}/E_{\mathrm{kin}} \leq 5 \times 10^{-3}$), with the measured growth rate listed in Table 4. The growth rate is slightly higher for USM-HLLD compared to USM-BK, which is consistent with the higher Prandtl number of USM-HLLD (see Table 5), similar to what we found for the Mach 0.1 comparison of the two solvers.

5.4.2 *Morphology*

Fig. 9 shows the kinetic energy, the magnetic energy, and the vorticity, respectively, in a slice during the kinematic phase when $E_{\mathrm{mag}}/E_{\mathrm{kin}} = 10^{-4}$. We see that more small-scale kinetic structure is captured in USM-BK compared to USM-HLLD. This is consistent with the fact that USM-BK dissipates kinetic energy at smaller length scales compared to USM-HLLD. The presence of small-scale structures (left panel) shows that smaller eddies are present in the USM-BK test case, whereas USM-HLLD dissipates energy into heat before forming eddies of comparable sizes. A similar pattern is hinted by the magnetic energy (middle panel), where USM-BK captures somewhat more small-scale structure than USM-HLLD. This difference is demonstrated quantitatively in the next section. Our findings are further corroborated by the vorticity modulus (right panel), where USM-BK captures $\sim 20\%$ more vorticity (see inset label) than USM-HLLD.

5.4.3 *Spectral analysis*

We repeat the analysis in Section 5.3.3 for the two Mach 0.01 runs. Fig. 10 shows the kinetic energy, magnetic energy, current, and vorticity power spectra. The kinetic spectra reveal that USM-HLLD turns downwards (a sign of the onset of dissipation) on scales larger (wave-numbers smaller) than USM-BK, implying that USM-BK dissipates kinetic energy at smaller length scales compared to USM-HLLD, and is therefore less dissipative. The current power spectrum peaks at a larger wave-number for USM-BK than USM-HLLD, implying that magnetic resistivity starts acting at smaller length scales for USM-HLLD compared to USM-BK, i.e., USM-HLLD is somewhat more resistive than USM-BK. The sharp downward turn of the vorticity power spectrum of USM-HLLD indicates that smaller eddies have been dissipated into heat, a consequence of smaller viscous dissipations wave-number. The fitted dissipation wave-numbers are reported in Table 4. We find that USM-BK dissipates at significantly smaller length scales both in terms of kinetics (58% difference in the wave-numbers) and magnetics (23% difference in the wave-numbers).

5.4.4 *Numerical Reynolds numbers*

Following the relations given in Appendix A, we measure the numerical hydrodynamic and magnetic Reynolds numbers, and the Prandtl number in Table 5. We find that USM-BK has $\mathrm{Re} = 800^{+380}_{-220}$, while USM-HLLD has $\mathrm{Re} = 240^{+140}_{-80}$, implying that the former is less dissipative. We note that the Re for USM-HLLD has dropped by a factor of 2.5, compared to the Mach 0.1 run, while USM-BK has roughly the same value, demonstrating that the solver successfully retains high values of Re even at low Mach number. The Pm for USM-BK is lower $\left(\mathrm{Pm} = 6.5^{+6.1}_{-3.3}\right)$ compared to USM-HLLD $\left(\mathrm{Pm} = 21^{+31}_{-12}\right)$, which explains why USM-BK has a lower growth rate in Table 4. Since Pm is so much higher in USM-HLLD, the product of Re and Pm, i.e., Rm, turns out to be similar for both solvers.

5.5 Computational Cost

Factoring out the sound speed (c_{s}) in Eq. (13) and approximating the Alfvén speed in the x-direction by the total Alfvén speed ($c_{\mathrm{A;x}} \approx c_{\mathrm{A}}$),

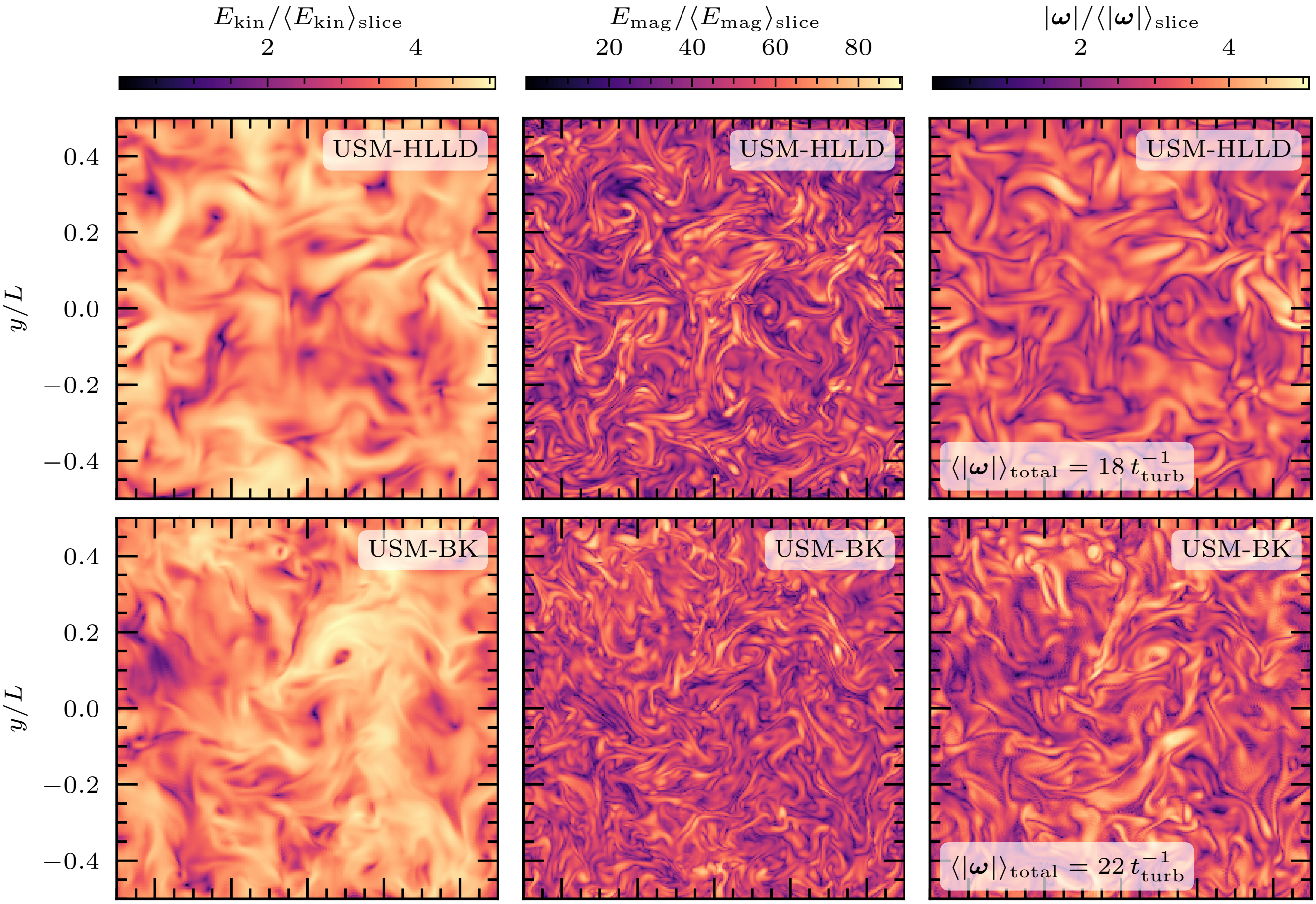

Figure 9. Slices of kinetic energy (left), magnetic energy (middle), and vorticity, $\boldsymbol{\omega} = \nabla \times \boldsymbol{v}$ (right), through the simulation domain taken during the kinematic phase of the turbulent dynamo at Mach 0.01 when $E_{\rm mag}/E_{\rm kin} = 10^{-4}$. The presence of small-scale structure in USM-BK shows that it dissipates kinetic energy at smaller length scales compared to USM-HLLD. Compared to the kinetic energy, the magnetic energy (middle panels) shows somewhat smaller qualitative differences between the two solvers, but it appears that also here the USM-BK captures slightly more small-scale turbulent structure than USM-HLLD; quantified in Section 5.4.3. Finally, the vorticity (right-hand panels) reinforces the finding that USM-BK captures more small-scale structure than USM-HLLD. The inset labels on the vorticity panels show measurements of the mean vorticity in the entire system (not just the slice), demonstrating that USM-BK captures $\sim 20\%$ more vorticity than USM-HLLD.

Table 4. Same as Tab. 2, but for Mach 0.01.

Name	$\Gamma(t_{\rm turb}^{-1})$	$p_{\rm bn}$	$k_{\rm bn}$	$\tilde{k}_\nu$	p_ν	k_ν	k_η
(1)	(2)	(3)	(4)	(5)	(6)	(7)	(8)
USM-HLLD	$2.09^{+0.02}_{-0.02}$	$0.3^{+0.2}_{-0.2}$	$2.0^{+0.7}_{-0.4}$	$2.6^{+0.8}_{-0.6}$	$0.8^{+0.1}_{-0.1}$	$3.1^{+0.8}_{-0.7}$	31^{+9}_{-6}
USM-BK	$1.94^{+0.01}_{-0.01}$	$-0.2^{+0.2}_{-0.2}$	$4.7^{+0.5}_{-0.5}$	$10.6^{+1.4}_{-1.4}$	$1.2^{+0.1}_{-0.1}$	$7.4^{+1.0}_{-0.6}$	40^{+5}_{-3}

Table 5. Same as Table 3, but for Mach 0.01.

Name	Re	Rm	Pm
(1)	(2)	(3)	(4)
USM-HLLD	$2.4^{+1.4}_{-0.8} \times 10^2$	$5.5^{+6.8}_{-3.1} \times 10^3$	21^{+31}_{-12}
USM-BK	$8.0^{+3.8}_{-2.2} \times 10^2$	$5.2^{+5.7}_{-2.7} \times 10^3$	$6.5^{+6.1}_{-3.3}$

we can write the fastest wave-speed as

$$\lambda_{\rm fastest} \approx c_{\rm s} M + \frac{c_{\rm s}}{2}\sqrt{\left(\frac{1}{M_{\rm BK}^2} + \frac{M^2}{M_{\rm A}^2}\right) + \sqrt{\left(\frac{1}{M_{\rm BK}^2} + \frac{M^2}{M_{\rm A}^2}\right)^2 - 4\frac{M^2}{M_{\rm A}}}}, \tag{29}$$

where $M_{\rm BK} = 1$ for conventional Riemann solvers, while $M_{\rm BK} \approx \mathcal{M}$ for the BK method, for our choice of $M_{\rm cut} = \mathcal{M}$. For our application of turbulent dynamos where $M \approx \mathcal{M} \ll 1 \ll \mathcal{M}_{\rm A} \approx M_{\rm A}$ and $c_{\rm s} \approx 1$, this can be written as

$$c_{\rm fastest} \sim \mathcal{M} + \frac{1}{M_{\rm BK}}\,. \tag{30}$$

We can immediately see that for conventional Riemann solvers, the fastest signal speed scales as $(1 + \mathcal{M}) \sim 1$ while for the BK method it scales as $\sim 1/\mathcal{M}$. Therefore, the time-step ($\Delta t \propto c_{\rm fastest}^{-1}$) is indepen-

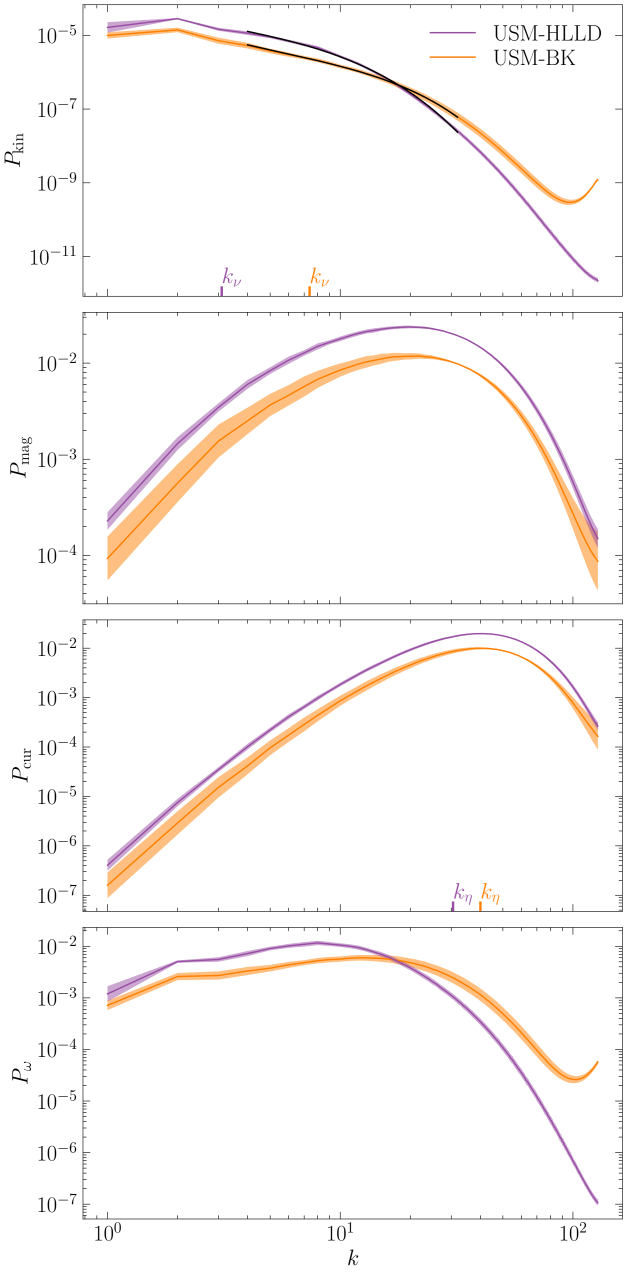

Figure 10. Time-averaged power spectra of the kinetic energy (top panel), magnetic energy (second panel), electric current (third panel) and vorticity (bottom panel), for USM-HLLD and USM-BK. USM-BK has been shifted by a factor of 0.5 along the y-axis for clarity. The black lines are the fits to the model given in Eq. (24). The viscous dissipation scale and resistive dissipation scale are marked on the x-axis. Both the viscous and resistive dissipation scales are significantly separated from each other, showing that USM-BK is less dissipative than USM-HLLD, in both kinetics and magnetics.

dent of the Mach number for conventional solvers, however, $\Delta t \propto \mathcal{M}$ for the BK method (see Eq. 15).

Since the turbulent turnover time ($t_{\rm turb}$) also scales as $\sim 1/\mathcal{M}$ (c.f., Sec. 5.2), the number of time-steps required to achieve the same amount of time evolution (i.e., the number of eddy-turnover times of evolution) also scales as $\sim 1/\mathcal{M}$. Therefore, the total cost of a simulation with the BK method scales as $1/\mathcal{M}^2$, while that for conventional Riemann solvers goes as $1/\mathcal{M}$. Therefore, an implicit implementation of the BK method, which is less restrictive in the time-step constraint, is preferable and we leave it to future works.

6 CONCLUSIONS

We examined the impact of numerical schemes, particularly the choice of Riemann solver, on numerical dissipation in low-Mach MHD simulations. Using the Balsara vortex test problem, we assessed the suitability of the new Riemann solver (USM-BK) and explored its effectiveness in capturing structures in low-Mach turbulent dynamo simulations. The following are the main conclusions drawn from this work:

(i) Conventional Riemann solvers (Roe, HLLC, HLLD, and Bouchut) exhibit excessive dissipation in the low-Mach regime.

(ii) The new USM-BK solver demonstrates the least dissipation of kinetic energy in the Balsara vortex tests at Mach 0.01, preserving 84% of the kinetic energy after one complete advection of the vortex across the computational grid. In constrast, USM-Roe, USM-HLLC, and USM-HLLD show the highest dissipation, preserving only 39% of the kinetic energy.

(iii) The USM-BK solver also exhibits the least dissipation of magnetic energy at Mach 0.01, retaining 99% of the magnetic energy after one complete advection of the Balsara vortex. It marginally outperforms USM-HLLD and USM-Roe, which retain 97% of the magnetic energy.

(iv) An unsplit-staggered mesh (USM) implementation of the BK Riemann solver is preferred over the usage of divergence cleaning since divergence cleaning also diffuses the magnetic energy. Furthermore, constrained transport keeps the divergence of magnetic field close to zero up to machine precision, by construction.

(v) The time-step restriction for stability for USM-BK scales as $\Delta t \sim O(\mathcal{M})$ (c.f., Eq. 15). Therefore, implicit time-steppers are preferable for applications in the low Mach regime.

(vi) As discussed in Section 5, the choice of Riemann solver significantly influences both the growth rate and the saturation level of the dynamo due to variations in the effective Reynolds numbers between solvers. We measured the growth rates and the corresponding effective Reynolds numbers for various solvers at Mach 0.1 and Mach 0.01.

(vii) The new solver can resolve smaller length scales compared to the other solvers, which is evident from the kinetic and electric current spectra. While USM-HLLD marginally outperforms USM-BK in resolving magnetic structures at Mach 0.1, USM-BK surpasses USM-HLLD in performance as the Mach number is decreased. This difference in dissipation length scales is also reflected in the morphological features seen in snapshots taken during the kinematic phase.

(viii) At a given energy ratio, USM-BK captures more vorticity compared to USM-HLLD. The vorticity power spectra show that USM-BK has more power at smaller wave-numbers than USM-HLLD, indicating that USM-BK captures more small-scale structures since smaller eddies have not been dissipated into heat.

We conclude that the new USM-BK solver is the most suitable for low-Mach MHD simulations, as it exhibits the least dissipation of kinetic and magnetic energy. The solver is particularly effective in capturing small-scale structures of the flow, making it ideal for turbulent dynamo simulations in the low-Mach regime.

ACKNOWLEDGEMENTS

We thank Knut Waagan for helpful discussions in the early stages of this work. C. F. acknowledges funding provided by the Australian Research Council (Discovery Project grants DP230102280 and DP250101526), and the Australia-Germany Joint Research Cooperation Scheme (UA-DAAD). We further acknowledge high-performance computing resources provided by the Leibniz Rechenzentrum and the Gauss Centre for Supercomputing (grants pr32lo, pr48pi, pn76ga and GCS Large-scale project 10391), the Australian National Computational Infrastructure (grant ek9) and the Pawsey Supercomputing Centre (project pawsey0810) in the framework of the National Computational Merit Allocation Scheme and the ANU Merit Allocation Scheme. The simulation software, `FLASH`, was in part developed by the Flash Centre for Computational Science at the University of Chicago and the Department of Physics and Astronomy at the University of Rochester. We also acknowledge the use of OpenAI's ChatGPT for assistance in proofreading and improving the clarity of the manuscript.

DATA AVAILABILITY

The data used in this article (approximately 4 TB) is available upon reasonable request to the authors.

REFERENCES

Achikanath Chirakkara R., Federrath C., Trivedi P., Banerjee R., 2021, Phys. Rev. Lett., 126, 091103

Balsara D. S., 2004, The Astrophysical Journal Supplement Series, 151, 149

Beattie J. R., Federrath C., Kriel N., Mocz P., Seta A., 2023, MNRAS, 524, 3201

Beck R., Wielebinski R., 2013, Magnetic Fields in Galaxies. Springer Netherlands, Dordrecht, pp 641–723, doi:10.1007/978-94-007-5612-0_13, `https://doi.org/10.1007/978-94-007-5612-0_13`

Berger M. J., Colella P., 1989, JournalofComputationalPhysics, 82, 64

Birke C., Klingenberg C., 2023, in Springer Proceedings in Mathematics & Statistics 433, Finite Volume and Complex Applications X—Volume 2, Hyperbolic and Related Problems. , doi:https://doi.org/10.1007/978-3-031-40860-1_5

Birke C., Chalons C., Klingenberg C., 2023, Communications in Mathematical Sciences, vol. 21, no. 8, p. 2213–2246

Birke C., Boscheri W., Klingenberg C., 2024, Journal of Scientific Computing, vol. 98, no. 34, p. arXiv:2306.16286

Boneva, D. V. Mikhailov, E. A. Pashentseva, M. V. Sokoloff, D. D. 2021, A&A, 652, A38

Brandenburg A., Subramanian K., 2005, Physics Reports, 417, 1

Choudhari A. R., 2015, Natures's third cycle: A story of sunspots. Oxford

Clerc S., 2000, Journal of Computational Physics, 161, 354

Dai W., Woodward P. R., 1998, The Astrophysical Journal, 494, 317

Dedner A., Kemm F., Kröner D., Munz C. D., Schnitzer T., Wesenberg M., 2002, Journal of Computational Physics, 175, 645

Dubey A., et al., 2008, in Pogorelov N. V., Audit E., Zank G. P., eds, Astronomical Society of the Pacific Conference Series Vol. 385, Numerical Modeling of Space Plasma Flows. p. 145

Eswaran V., Pope S. B., 1988, Computers and Fluids, 16, 257

Evans C. R., Hawley J. F., 1988, ApJ, 332, 659

Falkovich G., 1994, Physics of Fluids, 6, 1411

Federrath C., 2015, MNRAS, 450, 4035

Federrath C., 2016, Journal of Plasma Physics, 82, 535820601

Federrath C., Roman-Duval J., Klessen R. S., Schmidt W., Mac Low M. M., 2010, A&A, 512, A81

Federrath C., Schober J., Bovino S., Schleicher D. R. G., 2014, ApJ, 797, L19

Federrath C., Klessen R. S., Iapichino L., Beattie J. R., 2021, Nature Astronomy, 5, 365

Federrath C., Roman-Duval J., Klessen R. S., Schmidt W., Mac Low M. M., 2022, TG: Turbulence Generator, Astrophysics Source Code Library, record ascl:2204.001 (ascl:2204.001)

Fletcher A., Beck R., Shukurov A., Berkhuijsen E. M., Horellou C., 2011, Monthly Notices of the Royal Astronomical Society, 412, 2396

Frisch U., 1995, Turbulence, the legacy of A. N. Kolmogorov. Cambridge Univ. Press

Fryxell B., et al., 2000, ApJS, 131, 273

Gardiner T. A., Stone J. M., 2008, Journal of Computational Physics, 227, 4123

Guillard H., Murrone A., 2004, Computers & Fluids, 33, 655

Klein R., 1995, Journal of Computational Physics, 121, 213

Kriel N., Beattie J. R., Seta A., Federrath C., 2022, Monthly Notices of the Royal Astronomical Society, 513, 2457

Kriel N., Beattie J. R., Federrath C., Krumholz M. R., Hew J. K. J., 2023, arXiv e-prints, p. arXiv:2310.17036

Kupka F., Muthsam H. J., 2017, Living Reviews in Computational Astrophysics, 3, 1

Lee D., 2006, PhD thesis, University of Maryland, `http://hdl.handle.net/1903/3842`

Leggett J., Zhao Y., Sandberg R. D., 2022, Journal of Turbomachinery, 145

Leidi G., Birke C., Andrassy R., Higl J., Edelmann P. V. F., Wiest G., Klingenberg C., Röpke F. K., 2022, A&A, 668, A143

Li S., 2005, Journal of Computational Physics, 203, 344

Malvadi Shivakumar L., Federrath C., 2023, arXiv e-prints, p. arXiv:2311.10350

Marder B., 1987, Journal of Computational Physics, 68, 48

Miczek F., Röpke F. K., Edelmann P. V. F., 2015, A&A, 576, A50

Min M., et al., 2024, arXiv e-prints, p. arXiv:2409.19119

Minoshima T., Miyoshi T., 2021, Journal of Computational Physics, 446, 110639

Miyoshi T., Kusano K., 2005, Journal of Computational Physics, 208, 315

Park H., Linton D., Thornber B., 2022, International Journal of Heat and Fluid Flow, 93, 108916

Penna R. F., McKinney J. C., Narayan R., Tchekhovskoy A., Shafee R., McClintock J. E., 2010, Monthly Notices of the Royal Astronomical Society, 408, 752

Roe P., 1981, Journal of Computational Physics, 43, 357

Ruzmaikin A. A., Sokolov D. D., Shukurov A. M., 1988, Magnetic Fields of Galaxies. Astrophysics and Space Science Library Vol. 133, Springer Dordrecht, doi:10.1007/978-94-009-2835-0

Schekochihin A. A., Cowley S. C., Maron J. L., McWilliams J. C., 2004, Phys. Rev. Lett., 92, 054502

Schmidt W., Hillebrandt W., Niemeyer J. C., 2004, arXiv e-prints, pp astro–ph/0407616

Seta A., Federrath C., 2020, MNRAS, 499, 2076

Seta A., Federrath C., 2022, Monthly Notices of the Royal Astronomical Society, 514, 957

Sharda P., Federrath C., Krumholz M. R., Schleicher D. R. G., 2021, MNRAS, 503, 2014

Tissot G., Mémin É., Jamet Q., 2023, arXiv e-prints, p. arXiv:2309.12077

Turkel E., 1999, Annual Review of Fluid Mechanics, 31, 385

Verma M. K., Donzis D., 2007, Journal of Physics A: Mathematical and Theoretical, 40, 4401

Waagan K., Federrath C., Klingenberg C., 2011, Journal of Computational Physics, 230, 3331

Wagstaff J. M., Banerjee R., Schleicher D., Sigl G., 2014, Phys. Rev. D, 89, 103001

Yee K., 1966, IEEE Transactions on Antennas and Propagation, 14, 302

van Leer B., 1984, SIAM Journal on Scientific and Statistical Computing, 5, 1

APPENDIX A: EFFECTIVE HYDRODYNAMIC AND MAGNETIC REYNOLDS NUMBERS

The hydrodynamic Reynolds number (Re) is defined as

$$\mathrm{Re} = \frac{u_{\mathrm{turb}}\ell_{\mathrm{turb}}}{\nu}, \tag{A1}$$

where u_{turb} is the fluid turbulent velocity at the driving scale of turbulence ($\ell_{\mathrm{turb}} = 2\pi/k_{\mathrm{driving}}$) and ν is the kinematic viscosity of the fluid. Similarly, the magnetic Reynolds number (Rm) is defined as

$$\mathrm{Rm} = \frac{u_{\mathrm{turb}}\ell_{\mathrm{turb}}}{\eta}, \tag{A2}$$

where η is the magnetic resistivity of the fluid.

Numerical viscosity and resistivity must be lower than the explicit viscosity and resistivity to avoid smearing of features and over-damping of flows. Therefore, the numerical Reynolds numbers associated with a numerical scheme must be greater than the explicit Reynolds number being simulated. We can calculate the numerical Hydrodynamic Reynolds number and Magnetic Prandtl number of ideal MHD simulations from measurements of the characteristic dissipation scales.

To calculate the hydrodynamic Reynolds number, we use the following relation given in Kriel et al. (2022)

$$\mathrm{Re} = \left(\frac{k_\nu}{c_\nu k_{\mathrm{driving}}}\right)^{4/3}, \tag{A3}$$

where $c_\nu = 0.025^{+0.005}_{-0.006}$ (referred to as c_{Re} in the main text).

To measure the magnetic Reynolds number, we follow Kriel et al. (2023). However, their definition of the resistive dissipation scale (their definition will be referred to as k'_ν) is different from what we have used in Eq. (24). They define the viscous dissipation wavenumber as the wave-number where the scale-dependent hydrodynamic Reynolds number equals one, i.e., $\mathrm{Re}(k'_\nu) = 1$. This wavenumber marks the scale where the flow transitions from an inertial force dominated one ($k_{\mathrm{turb}} < k < k'_\nu$) to a dissipation-dominated one ($k > k'_\nu$). Kriel et al. (2023) have shown that k'_ν and Re are related by

$$k'_\nu = c'_\nu k_{\mathrm{driving}} \mathrm{Re}^{3/4}, \tag{A4}$$

where $c'_\nu = 0.10^{+0.01}_{-0.01}$.

Using Eq. (A3) and Eq. (A4), we can write

$$k'_\nu = \frac{c'_\nu}{c_\nu} k_\nu. \tag{A5}$$

Thus, if we have measured k_ν from spectral fitting in Eq. (24), we can find k'_ν.

Kriel et al. (2023) have also shown the resistive dissipation wavenumber (k_η) scales with the viscous dissipation wave-number (k'_ν, based on the alternative definition mentioned here) and the Prandtl number as

$$k_\eta = c_\eta k'_\nu \mathrm{Pm}^{1/2}, \tag{A6}$$

where $c_\eta = 0.53^{+0.07}_{-0.07}$.

Using Eq. (A5) and Eq. (A6), we can write

$$k_\eta = c_\eta \frac{c'_\nu}{c_\nu} k_\nu \mathrm{Pm}^{1/2} = c_{\mathrm{Pm}} k_\nu \mathrm{Pm}^{1/2}, \tag{A7}$$

where $c_{\mathrm{Pm}} = c_\eta c'_\nu / c_\nu = 2.1^{+0.8}_{-0.5}$.

The Prandtl number (Pm) can be obtained using the above relation. The Magnetic Reynolds number can then be calculated as

$$\mathrm{Rm} = \mathrm{Re} \times \mathrm{Pm}. \tag{A8}$$

This paper has been typeset from a TEX/LATEX file prepared by the author.